





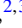

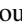
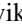

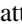
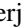


Epitaxial growth, magnetoresistance, and electronic band structure of GdSb magnetic semimetal films

Hadass S. Inbar ^{1,*} Dai Q. Ho ^{2,3} Shouvik Chatterjee ^{4,†} Mihir Pendharkar ^{4,‡} Aaron N. Engel ¹ Jason T. Dong,¹ Shoaib Khalid ^{2,§} Yu Hao Chang ¹ Taozhi Guo,^{1,||} Alexei V. Fedorov ⁵ Donghui Lu ⁶ Makoto Hashimoto ⁶ Dan Read ^{4,7} Anderson Janotti ² and Christopher J. Palmström ^{1,4,¶}

¹Materials Department, University of California Santa Barbara, Santa Barbara, California 93106, USA

²Department of Materials Science and Engineering, University of Delaware, Newark, Delaware 19716, USA

³Faculty of Natural Sciences, Quy Nhon University, Quy Nhon 59000, Vietnam

⁴Electrical and Computer Engineering Department, University of California Santa Barbara, Santa Barbara, California 93106, USA

⁵Advanced Light Source, Lawrence Berkeley National Laboratory, Berkeley, California 94720, USA

⁶Stanford Synchrotron Radiation Lightsource, SLAC National Accelerator Laboratory, 2575 Sand Hill Road, Menlo Park, California 94025, USA

⁷School of Physics and Astronomy, Cardiff University, Cardiff CF24 3AA, United Kingdom



(Received 5 August 2022; accepted 20 October 2022; published 9 December 2022)

Motivated by observations of extreme magnetoresistance (XMR) in bulk crystals of rare-earth monopnictide (RE-V) compounds and emerging applications in novel spintronic and plasmonic devices based on thin-film semimetals, we have investigated the electronic band structure and transport behavior of epitaxial GdSb thin films grown on III-V semiconductor surfaces. The Gd^{3+} ion in GdSb has a high spin $S = 7/2$ and no orbital angular momentum, serving as a model system for studying the effects of antiferromagnetic order and strong exchange coupling on the resulting Fermi surface and magnetotransport properties of RE-Vs. We present a surface and structural characterization study mapping the optimal synthesis window of thin epitaxial GdSb films grown on III-V lattice-matched buffer layers via molecular-beam epitaxy. To determine the factors limiting XMR in RE-V thin films and provide a benchmark for band-structure predictions of topological phases of RE-Vs, the electronic band structure of GdSb thin films is studied, comparing carrier densities extracted from magnetotransport, angle-resolved photoemission spectroscopy (ARPES), and density-functional theory (DFT) calculations. ARPES shows a hole-carrier rich, topologically trivial, semimetallic band structure close to complete electron-hole compensation, with quantum confinement effects in the thin films observed through the presence of quantum-well states. DFT-predicted Fermi wave vectors are in excellent agreement with values obtained from quantum oscillations observed in magnetic field-dependent resistivity measurements. An electron-rich Hall coefficient is measured despite the higher hole-carrier density, attributed to the higher electron Hall mobility. The carrier mobilities are limited by surface and interface scattering, resulting in lower magnetoresistance than that measured for bulk crystals.

DOI: [10.1103/PhysRevMaterials.6.L121201](https://doi.org/10.1103/PhysRevMaterials.6.L121201)

I. INTRODUCTION

In recent years, topological and trivial semimetals have received renewed interest due to observations of extremely large magnetoresistance (XMR) [1], which can be used in novel

magnetic sensing technologies [2]. In topological semimetals, exotic transport characteristics due to the relativistic nature of charge carriers also hold great promise for applications in spintronic devices [3,4]. The coupling between antiferromagnetic order and relativistic quasiparticles offers new possibilities to control the symmetry of topological states and their spin-polarized currents by manipulating the magnetization orientation [5,6]. New spin-orbitronic devices based on current-induced Néel spin-orbit torques could dissipate less energy and perform at high switching rates [7]. Applications of antiferromagnetic topological crystals and magnetic topological heterostructures include spin valves [8,9], THz photodetectors [10–12], and recent studies are also exploring the design of heterogeneous catalysts leveraging the robust metallic surface states and spin polarization in electron transfer reactions [13–15].

Rare-earth monopnictides (RE-Vs) are a class of semimetals that can be easily integrated with III-V semiconductors

*hadass@ucsb.edu

†Present address: Department of Condensed Matter Physics and Materials Science, Tata Institute of Fundamental Research Mumbai 400005, India.

‡Present address: Department of Materials Science and Engineering, Stanford University, Stanford, CA 94305, USA.

§Present address: Department of Physics, School of Natural Sciences, National University of Science and Technology, Islamabad 44000, Pakistan.

||Present Address: Department of Physics, Princeton University, Princeton, New Jersey, 08540, USA.

¶cjpalms@ucsb.edu

[16–18] and present XMR [19], nontrivial topology [20], Fermi arcs [21], and unique magnetic phase diagrams [22] due to strong p - f and d - f electron coupling. The wide range of lattice constants, high thermodynamic stability, and the similarity of the rocksalt structure of RE-Vs with zincblende III-V semiconductors allow them to be incorporated epitaxially and processed into scalable devices [18,23,24]. The III-V/RE-V magnetoresistive hybrid structures could utilize the geometric contribution to the extraordinary magnetoresistance found in high-mobility III-V–metal interfaces [25] and the tunability of conductivity in RE-Vs to optimize the heterostructure material parameters [26].

Many RE-Vs possess large nonsaturating magnetoresistance, attributed to charge-carrier compensation and the nearly equal electron and hole high mobilities leading to a parabolic rise in magnetoresistance based on a classical two-band model [27,28]. To date, most thin-film reports of magnetoresistance values in RE-V [29,30] and other XMR semimetals [31] are significantly lower than their bulk crystal counterparts, potentially due to diminished mobilities as a result of surface and defect scattering, as well as possible deviations from exact mobility matching and carrier compensation. To explore the potential for novel RE-V semimetal devices, it is necessary to map the electronic structure of RE-V thin films and study the degrees of freedom that could help tune magnetoresistance, such as magnetic order transitions, quantum confinement effects, and defect scattering. From a thin-film synthesis perspective, GdSb is relatively straightforward to grow epitaxially on III-V semiconductors. Lighter rare-earth elements tend to be more reactive [32] and form more stable competing RE-Sb₂ phases [33].

Apart from magnetoresistive devices, synthesizing RE-Vs as thin films subject to biaxial strain and confinement effects also presents an opportunity to tune their band-structure topology. While only RE-V bulk crystals with high spin-orbit coupling and large lattice parameters ($X\text{Bi}$, $X = \text{La-Gd}$) were found to host topological semimetal states [34–36], recent studies suggest that Sb- and As-based RE-Vs subject to high pressure could also transition into a nontrivial topological phase [37,38]. Having a lattice parameter $a = 6.219 \text{ \AA}$ [39], GdSb is uniquely positioned between InSb (6.4794 \AA) and GaSb (6.0959 \AA)/AlSb (6.1355 \AA), allowing tensile and compressive biaxial strain to be tuned by the underlying semiconducting III-V buffer layer structure. Further, epitaxial films of GdSb can serve as high-quality buffer layers that also aid as diffusion barriers for integrating reactive layers on III-V semiconductors [40]. The synthesis of thin films of GdSb also opens up more opportunities to study quantum size effects in RE-Vs, where quantum confinement was shown to alter carrier compensation and differentially affect the mobility of the electron- and holelike carriers [29,30,41]. In addition to improving the fundamental understanding of magnetotransport properties in GdSb, our electronic structure study can be used to engineer plasma resonance frequencies in RE-Vs and semimetal films for plasmonic midinfrared optoelectronic applications [42].

Here, we report the growth, ARPES, and magnetotransport of epitaxial lattice-matched GdSb films grown on III-V buffer layers via molecular-beam epitaxy (MBE). We report the synthesis conditions and electronic properties of epitaxial GdSb thin films. As a member of the RE-V family, GdSb

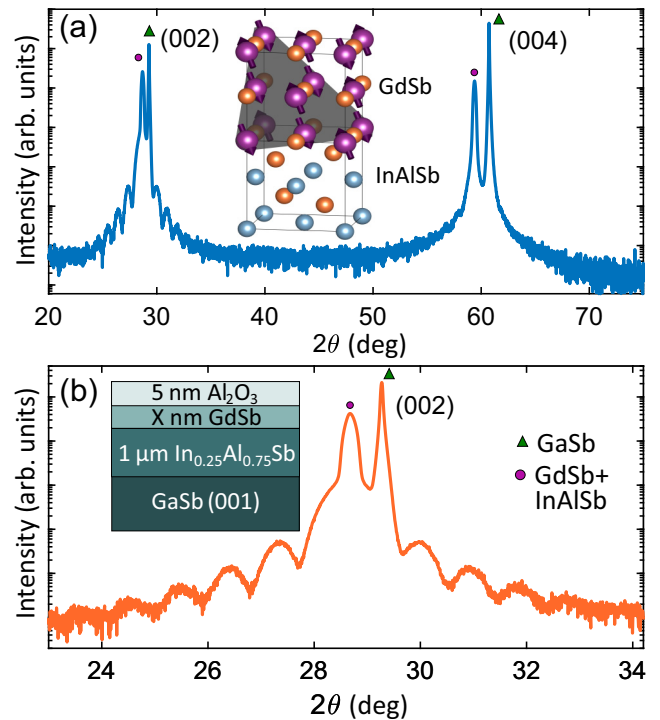


FIG. 1. (a) Out-of-plane θ - 2θ XRD scan for a 10-nm lattice-matched GdSb film grown on InAlSb/GaSb (001). The InAlSb and GdSb layers are indexed with a circle, the GaSb substrate with a triangle. (Inset) Crystal structure and epitaxial relationship of the GdSb/III-V structure, with the magnetic structures for the type-II AFM ground state of GdSb shown. (b) Zoom-in on the (002) reflection; inset shows the sample heterostructure.

shares the common features of antiferromagnetic ordering [43] and an unusually high magnetoresistance [39], with previous magnetotransport reports of GdSb bulk crystals presenting magnetoresistance values up to 12 500% [39]. Gd-V compounds serve as favorable model systems for studying magnetoresistive and magnetic scattering behavior in RE-V semimetals due to a relatively simple magnetic phase diagram, lack of orbital angular momentum, and deep-lying occupied $4f$ bands leading to a smaller p - f mixing than observed in Ce-Vs [22]. GdSb is a classical Heisenberg antiferromagnet (AFM), where Gd^{3+} ions with $S = 7/2$, $L = 0$ order as a type-II AFM at 24 K [43,44], such that the Gd magnetic moments are ordered ferromagnetically along the $\langle 11\bar{2} \rangle$ directions, and adjacent $\{111\}$ planes are coupled antiferromagnetically [see Fig. 1(a), inset]. The magnetic phase diagram of GdSb has an AFM phase that transitions to a spin-flop phase at very low fields (0.2 T at 4 K, $B \parallel (001)$). As the magnetic field increases, the spin-flop phase remains stable and linearly increases in magnetization until a critical field of 34.5 T is reached [43].

II. MBE GROWTH AND EXPERIMENT METHODS

The GdSb films were grown in a modified VG V80H III-V MBE growth chamber with a base pressure $< 5 \times 10^{-11}$ Torr. For magnetotransport measurements, epitaxial semi-insulating GaSb (001) wafers were used, with significant charge-carrier freeze-out expected below 80 K. For photoemission and scanning tunneling microscopy (STM)

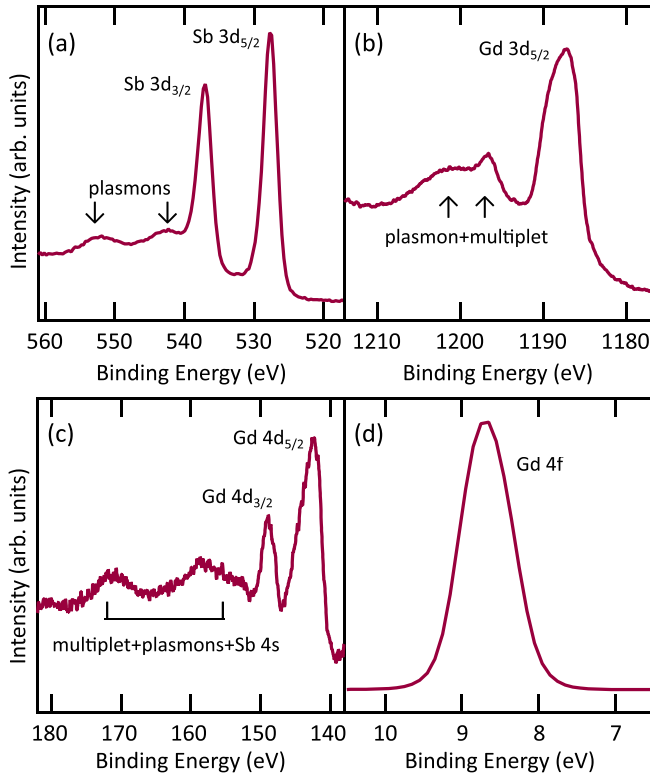


FIG. 2. *In situ* XPS of the (a) Sb $3d$, (b) Gd $3d_{5/2}$, (c) and Gd $4d$ core levels (d) ultraviolet photoemission spectroscopy (UPS) scan of the Gd $4f$ core level collected for *in vacuo* transferred GdSb films.

studies, conductive p -type Zn:GaSb (001) wafers were used, followed by p -type Be-doped III-V buffer layers. Surface reconstructions were monitored *in situ* with reflection high-energy electron diffraction (RHEED, Supplemental Material, Fig. S1 [45]).

Coherent growth of lattice-matched films was studied *in situ* with RHEED and confirmed *ex situ* with x-ray diffraction (XRD) measurements. Streaky RHEED patterns were seen for all layers, suggesting smooth and epitaxial films. Surface cleanliness, stoichiometry, and Gd speciation were monitored with *in situ* x-ray photoelectron spectroscopy (XPS). XPS analysis of the Gd $4d$, $3d$, and Sb $3d$ core levels in Figs. 2(a)–2(c) confirms stoichiometry is achieved (Sb : Gd = 1.04 : 1, within the uncertainty of XPS without a reference standard sample and accounting for the photoemission cross sections). The Gd $3d$ and $4d$ spectra and loss features are consistent with previous XPS studies of bulk GdSb [46]. The GdSb films did not show any signs of contamination *in vacuo*, i.e., the oxygen and carbon levels at the surface were below the XPS detection limit.

Following growth and before removal from vacuum, the GdSb films were protected from degradation in the air by capping in another interconnected vacuum system with an amorphous AlO_x layer deposited by e-beam evaporation of Al_2O_3 at room temperature. A schematic of a typical heterostructure grown for magnetotransport measurements is shown in Fig. 1. More details on thin-film preparation, and the experimental growth window for GdSb are found in Supplemental Material, Note 1 [45].

Vacuum ultraviolet (VUV)-light ARPES measurements in the 20–100 eV range were performed on 4- and 20-nm-thick (i) *in vacuo* transferred GdSb films, and (ii) Sb-capped, air-exposed, and Sb-decapped GdSb films. A custom-built vacuum suitcase with a base pressure $< 1 \times 10^{-10}$ Torr was used for transferring films from the growth chamber at University of California, Santa Barbara, to beamline 10.0.1.2 at the Advanced Light Source (ALS) in Berkeley. At the SLAC National Accelerator Laboratory, Sb-capped films were studied at beamline 5-2 at the Stanford Synchrotron Radiation Lightsource. Ultraviolet photoemission spectra of the Gd $4f$ and Sb $4d$ core levels were collected for the *in vacuo* ALS transferred GdSb films and the SLAC Sb-capped films (after Sb desorption). We confirmed the chemical stability of the GdSb films in both cases by the absence of any oxidized components or oxygen $2s$ peak. In Fig. 2(d), a single Gd $4f$ peak is observed at 8.68 eV, indicating no oxidation.

We investigated the electronic structure of GdSb theoretically using density functional theory (DFT) and the screened hybrid functional of Heyd, Scuseria, and Ernzerhof (HSE06) [47,48] with 25% of exact exchange and accounting for spin-orbit coupling, as implemented in the VASP code [49,50]. The $4f$ electrons were treated as valence electrons for the ferromagnetic (FM) and AFM calculations, whereas for the nonmagnetic phase calculation, the $4f$ electrons were treated as core electrons. We used the experimental lattice parameter of 6.219 Å for GdSb [39]. Additional details on the DFT calculations, ARPES data acquisition, and analysis are provided in Supplemental Material, Note 2 [45].

III. RESULTS AND DISCUSSION

A. Surface and structural characterization

Figure 1(a) shows a wide-range θ - 2θ XRD scan of the GdSb film grown on a GaSb (001) substrate and $\text{In}_{0.25}\text{Al}_{0.75}\text{Sb}$ (referred to as InAlSb) buffer layer, revealing no additional peaks from impurity phases. A higher-resolution triple-axis XRD scan near the (002) peak in Fig. 1(b) shows exact out-of-plane lattice matching between the GdSb film and the InAlSb metamorphic buffer layer. The Pendellösung fringes indicate abrupt interfaces, and the extracted GdSb thickness values agree with *in situ* flux calibrations using RHEED oscillation.

The surface morphology and nucleation of the GdSb films were studied at room temperature with *in situ* scanning tunneling microscopy (STM) and *ex situ* atomic force microscopy (Fig. 3). In Fig. 3 a cross-hatched pattern originates from misfit dislocations in the underlying relaxed InAlSb buffer layer. The thin AlSb layer between the GdSb film and InAlSb buffer layer was added in an effort to expand the GdSb growth window to higher temperatures and lower Sb flux [Fig. S1(h)] while mitigating any potential Gd-In interfacial exchange reactions [32] or displacement of In atoms to the surface [51]. Figures 3(c) and 3(d) show a decrease in the surface roughness of 30-nm GdSb films grown with an AlSb interlayer, suggesting the higher stability of the AlSb surface at low Sb_2 overpressure could play a role in high-quality GdSb growth (see Supplemental Material, Note 1 [45]). A relatively flat surface is achieved for the metamorphic buffer layer grown at low temperatures, as measured with *in situ* STM in Fig. 3(a). From

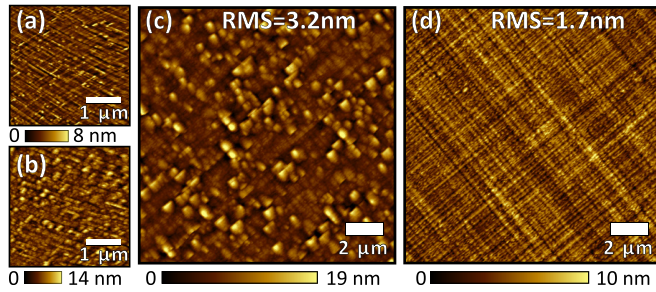


FIG. 3. *In situ* STM images of (a) III-V lattice-matched buffer layer: 2-nm AlSb/200-nm $\text{In}_{0.25}\text{Al}_{0.75}\text{Sb}/\text{GaSb}$ (001), and (b) 30-nm-thick GdSb grown on the lattice-matched buffer-layer structure. *Ex situ* atomic force microscope image of Al_2O_3 capped 30-nm GdSb films grown on the $\text{In}_{0.25}\text{Al}_{0.75}\text{Sb}$ layer (c) without and (d) with an AlSb interlayer.

the similar topography range in Figs. 3(b)–3(d), a thickness of 5 nm of the amorphous Al_2O_3 capping layer appears to passivate the GdSb surface well, without continuing reactions after removing the sample from a vacuum environment.

B. ARPES and DFT calculations

ARPES measurements performed for a 20-nm-thick GdSb film are presented in Figs. 4 and 5. In Fig. 4(b), we observe an ellipsoidal electron pocket (α) at the bulk X point, two nearly spherical light-hole (β) and spin-orbit split-off bands (γ) at the bulk Γ point, and a warped heavy-hole band (δ) resembling a square Fermi surface. The Fermi surface of the GdSb film is consistent with previous reports for other RE-Vs [27,35,36,52–54] and our DFT calculations in Fig. 4(g). Fits to all bulk bands near the Fermi level are presented in Fig. 5, and the resulting Fermi wave vector values and calculated carrier densities (Table I) are compared against DFT-extracted values (Table II). The ARPES Fermi wave vectors are closer to the AFM-phase DFT predictions than the nonmagnetic phase. The ARPES Fermi wave vectors are closer to the AFM-phase DFT predictions than the nonmagnetic phase. Based on the estimated Fermi volumes from the ARPES data, the 20-nm-thick GdSb film shows similar hole and electron carrier densities, with an electron/hole ratio of $n_e/n_h = 0.84$. The 4-nm-thick GdSb films studied with ARPES showed a similar semimetallic band structure.

The 20-nm-thick GdSb film displays multiple quantum-well states in the hole bands [in Figs. 4(c) and 4(d)] and particularly visible near $\bar{\Gamma}$ for the γ pocket and \bar{M} for the δ pocket in Figs. 5(a)–5(d)] and electron pockets [Figs. 4(e) and 5(e)–5(h)], confirming smooth conformal growth. At 20 nm, the GdSb film is still not at the bulk limit for all charge carriers, evidenced by the high number (>10) of finely spaced quantum-well subbands in the δ hole pocket. The electron pocket shows fewer subbands crossing the Fermi level with a larger energy separation [Fig. 4(e)] due to the smaller effective mass along the minor axis of the ellipsoidal electron pocket, suggesting that the electron band is strongly affected by quantum confinement.

Measurements of the electron pocket [Fig. 4(e)] along $\bar{\Gamma} - \bar{M} - \bar{\Gamma}$ show both the expected $W - X_1 - W$ band dispersion from the $k_z = \Gamma$ zone center along the minor axis, as well as the neighboring Brillouin-zone electron-pocket band dispersions at $k_z = X_3$ along the electron-pocket major axis

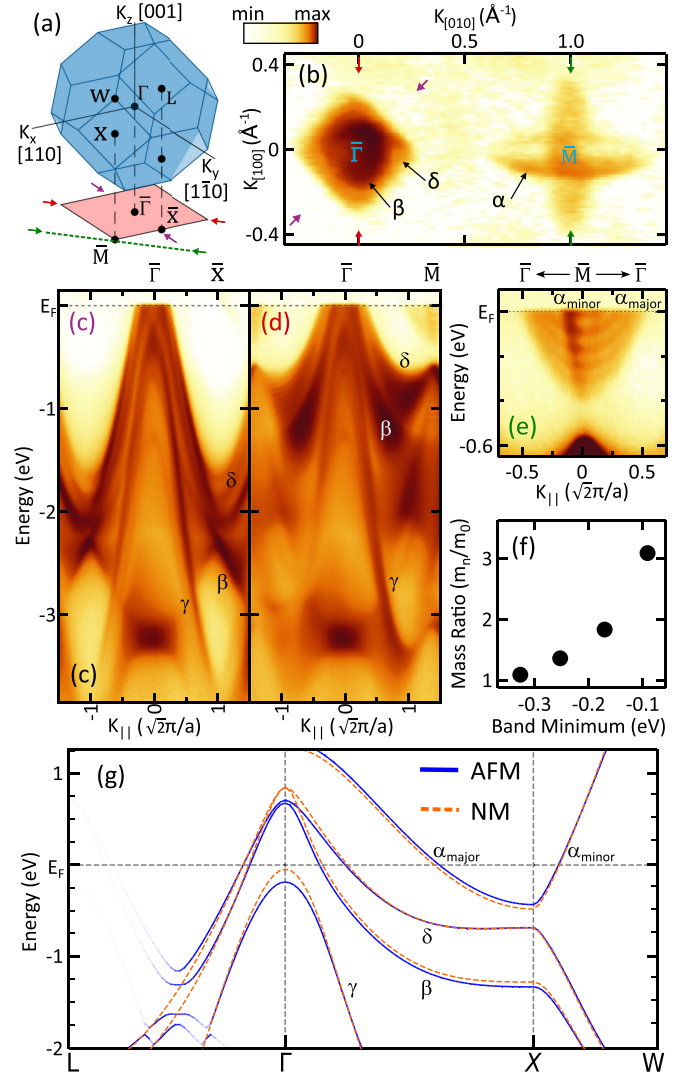


FIG. 4. (a) Rocksalt bulk three-dimensional Brillouin zone and (001) surface projection, with E - k scan directions in panels (c)–(e) highlighted with arrows along $\bar{X} - \bar{\Gamma} - \bar{X}$ (purple, c), $\bar{M} - \bar{\Gamma} - \bar{M}$ (red, d), and $\bar{\Gamma} - \bar{M} - \bar{\Gamma}$ (green, e). (b) $h\nu = 60$ eV ($k_z = \Gamma$) photoemission intensity plots at E_F showing the Fermi surface map displaying holelike bands (β , δ) and electron-like (α) bands. (c), (d) Band dispersion of the hole pockets and (e) the electron pocket, presenting quantum-well states in all three bands. (f) Relative mass enhancement of the electrons in the quantum-well subbands (m_n) with respect to the lowest level mass (m_0) as a function of the band minimum energy. (g) DFT-calculated band structure of GdSb in the antiferromagnetic (AFM), and nonmagnetic (NM) states. The AFM gap is predicted to form along the $\langle 111 \rangle$ direction and the spectral weight of the AFM folded band along $\bar{\Gamma} - L$ is reflected in the line transparency.

$\bar{\Gamma} - X_2 - \bar{\Gamma}$. The nearly identical dispersions along the major axis of the electron pocket at different photon energies in Figs. 5(e)–5(h) result from the high- k_z broadening expected for the VUV light used in the ARPES measurements [36].

In Fig. 4(f), the electron-pocket effective mass enhancement along the major elliptical axis is calculated for the first four subbands near the Fermi level. Since thick GdSb films are expected to have weak electron correlation effects, the

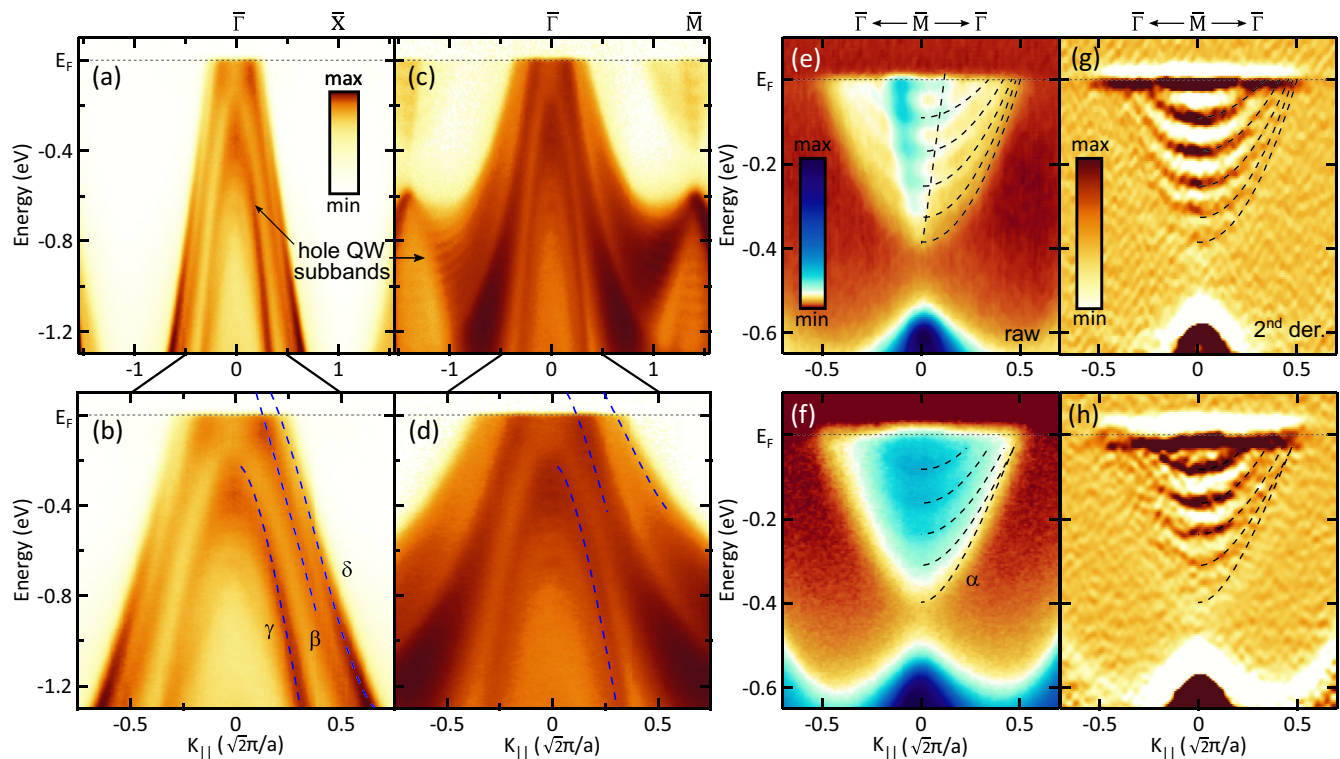


FIG. 5. ARPES data and overlaid fit to the bands for positive wave vectors. The β , γ , and δ hole pockets along (a), (b) $\bar{X} - \bar{\Gamma} - \bar{X}$ and (c), (d) $\bar{M} - \bar{\Gamma} - \bar{M}$. The α electron-pocket minor axis and major axis subbands along $\bar{\Gamma} - \bar{M} - \bar{\Gamma}$ at the (e) Γ plane ($h\nu = 60$ eV) and (f) X plane ($h\nu = 94$ eV). (g), (h) Second-derivative plots $\frac{\partial^2 I}{\partial E^2}$ of (e), (f), respectively, enhancing the dispersive features of the raw data.

enhanced mass in the subbands with minima closer to the Fermi level is explained by the highly linear and nonparabolic dispersion of the electron pocket. A similar trend was recently observed for IrO_2 [55]. The ability to alter the total carrier density and average effective carrier mass in GdSb quantumwells through thickness tuning suggests another route to controlling magnetoresistance in RE-V thin films [56].

The DFT HSE06 band structure calculations for the AFM and nonmagnetic phases are presented in Fig. 4(g) and appear to overlap at the Fermi level. The HSE06 AFM calculations matched our ARPES measurements and were shown to accurately describe the carrier concentrations and electronic band gap at the bulk X point compared to other functionals [54,57]. See Tables I and II for a comparison of ARPES and DFT

Fermi wave vectors and band extrema at the X - and Γ high-symmetry points. The electron-hole band gap at the bulk X point [Figs. 5(e) and 5(f)] is found to be $E_\alpha(X) - E_\delta(X) = 0.21$ eV and is in close agreement with the AFM phase HSE06 calculations predicting a gap of 0.25 eV in Fig. 4(g). Near Γ , we see the most significant deviation between the AFM and nonmagnetic band-structure calculations. In the nonmagnetic phase calculations, the spin-orbit coupled split-off $p_{1/2}(\gamma)$ pocket nearly crosses the Fermi level. However, as experimentally observed in Figs. 5(a)–5(d), the γ pocket-band maxima at the Γ point lies 0.19 eV below the Fermi level, showing that the predictions of the AFM phase (treating the p - f interactions explicitly) are in better agreement with experiments.

TABLE I. Fermi surface of a 20-nm-thick GdSb film. Band extrema energy positions, Fermi wave vectors, k_f , effective masses (m^*), and charge-carrier densities (n) obtained from the ARPES measurements. Further details provided in the Appendix and Supplemental Material, Note 2 [45].

Fermi surface	Band extrema (eV)			k_F (\AA^{-1})	m^* (m_0)	n (10^{20}cm^{-3})
	Γ	X				
α	NA	$-0.39(\pm 0.01)$	Minor	$0.084(\pm 0.014)$	Minor	$0.13(\pm 0.03)$
			Major	$0.36(\pm 0.03)$	Major	$1.73(\pm 0.29)$
γ	$-0.21(\pm 0.01)$	$-3.12(\pm 0.01)$	Does not cross the Fermi level			
β	NA	$-1.37(\pm 0.01)$	$\bar{\Gamma} - \bar{M}$	$0.10(\pm 0.01)$	$\bar{\Gamma} - \bar{M}$	$0.19(\pm 0.02)$
			$\bar{\Gamma} - \bar{X}$	$0.100(\pm 0.003)$	$\bar{\Gamma} - \bar{X}$	$0.17(\pm 0.01)$
δ	$0.31(\pm 0.06)$	$-0.60(\pm 0.01)$	$\bar{\Gamma} - \bar{M}$	$0.23(\pm 0.03)$	$\bar{\Gamma} - \bar{M}$	$0.40(\pm 0.08)$
			$\bar{\Gamma} - \bar{X}$	$0.170(\pm 0.002)$	$\bar{\Gamma} - \bar{X}$	$0.28(\pm 0.01)$

TABLE II. Band energies and Fermi wave vectors obtained from DFT HSE06 calculations for (a) the nonmagnetic phase, (b) AFM phase, and (c) the FM phase (spin up/down bands, accordingly). Carrier densities extracted from the DFT density of states of the nonmagnetic phase are compared against the analytical calculation of carrier density using the ellipsoid model for the electron pocket, and the sphere model for the hole bands (marked with *). Further details provided in the Appendix and Supplemental Material, Note 2 [45].

Fermi surface	Band extrema (eV)			k_F (\AA^{-1})	n (10^{20}cm^{-3})
	Γ	X			
α	NA	(a) -0.48 (b) -0.43 (c) $-0.13/-0.61$	Minor, major	(a) 0.103, 0.402 (b) 0.101, 0.383 (c) 0.054/0.111, 0.205/0.461	(a) 4.20 (4.32*), (c) 3.61
γ	(a) -0.05 , (b) -0.19 (c) $-0.13/-0.26$	(a) -3.31 , (b) -3.30 (c) $-3.15/-3.33$	Does not cross the Fermi level		
β	(a) 0.85 (b) 0.67 (c) 0.74/0.44	(a) -1.28 (b) -1.33 (c) -1.29	$\bar{M} - \bar{\Gamma}$ $\bar{X} - \bar{\Gamma}$	(a) 0.151, (b) 0.139, (c) 0.140, 0.133 (a) 0.144, (b) 0.139, (c) 0.148/0.125	(a) 1.18 (1.08*), (c) 0.92
δ	(a) 0.85 (b) 0.67 (c) 1.04/0.91	(a) -0.68 (b) -0.68 (c) -0.63	$\bar{M} - \bar{\Gamma}$ $\bar{X} - \bar{\Gamma}$	(a) 0.254, (b) 0.244, (c) 0.255/0.255 (a) 0.187, (b) 0.183, (c) 0.193/0.178	(a) 3.01 (3.62*), (c) 2.68

As a type-II AFM, the electron pockets in GdSb are not expected to show any exchange splitting because of the $\{111\}$ orientation of the ferromagnetic planes. From the spectral weight for the AFM unfolded bands in Fig. 4(g), we can see the shadow-band intensity along the $\Gamma - L$ high-symmetry axis is faint near the Fermi level. This can be explained by the relatively weak potential induced by the localized Gd $4f$ spin structure and the itinerant Sb $5p$ electrons forming the valence band [58]. In our ARPES data, we see no sign of band folding across the AFM Brillouin-zone magnetic boundary (the $\Gamma - L$ axis projected onto $\bar{\Gamma} - \bar{X}$) in Fig. 4(c) despite conducting the measurement below the Néel temperature (20 K), possibly due to either short-range AFM ordering or a low photoionization cross section for the Gd $4f$ level at 60 eV. Nevertheless, evidence of the strong p - f mixing predicted to take place in GdSb near the Fermi level [59] is found by comparing the position of the valence bands in DFT calculations for the nonmagnetic phase versus the AFM phase. In the AFM phase, p - f mixing shifts the valence band downward and results in hole Fermi wave vectors which agree better with the experimental values.

Finally, DFT calculations of a forced ferromagnetic phase in GdSb (Fig. S4), which forms under high magnetic fields, predict significant exchange splitting in the electron d band almost leading to a p - d band crossing which would result in a nontrivial band topology and the emergence of Weyl points. Due to the low position of the potential band crossing with respect to the Fermi level (~ 0.5 eV), any Weyl physics contribution to transport is expected to be negligible.

C. Magnetotransport

The temperature dependence of the electrical resistivity for a 10-nm-thick GdSb (001) film is shown in Fig. 6(a). The total resistivity of the stack peaks at 135 K as the InAlSb buffer-layer charge carriers freeze out, indicating the GdSb film has become the lowest resistive path for transport. Upon further cooling, the resistivity adheres to the same trends observed for bulk RE-V crystals [60]: a linear decrease with tempera-

ture is observed down to the Néel temperature, where a kink in resistivity at $T = 25$ K ($T_N = 25.02$ and 24.55 K for 10- and 4-nm-thick films, respectively) is followed by a sharper decrease in resistivity. The kink and the sharp drop in resistivity below the Néel temperature indicate that spin-disorder scattering significantly contributes to the total resistivity close to the Néel temperature. Applying higher magnetic fields perpendicular to the film plane increases the resistivity, mainly at lower temperatures.

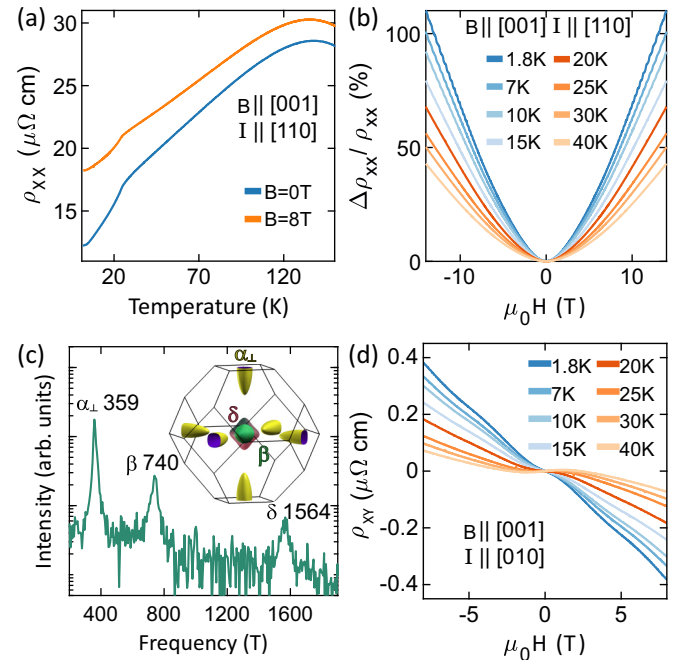


FIG. 6. Magnetotransport behavior of a 10-nm-thick GdSb film, (a) Temperature dependence of the longitudinal resistivity in the epitaxial stack. (b) Magnetoresistance vs magnetic field at temperatures below (blue) and near/above (orange) the Néel temperature. (c) Log plot of the FFT spectrum of SdH oscillations measured at 1.8 K. (Inset) GdSb Fermi surface. (d) Temperature dependence of the Hall resistivity.

TABLE III. Fermi surface parameters extracted from SdH oscillations for a 10-nm-thick GdSb film; calculations of the values are described in the Appendix and Supplemental Material, Note 3 [45].

Fermi surface	Frequency (Tesla)	k_F (\AA^{-1})	n (10^{20}cm^{-3})
α_{\perp} minor axis	359	0.104	4.32
β	740	0.150	1.14
δ	1564	0.251	5.34

The small Hall resistivity in Fig. 6(d) and high longitudinal resistivity upon applied magnetic field [Fig. 6(b)] both suggest that the films are stoichiometric and have a low defect concentration [39]. Macroscopic scattering sites in LuSb thin films have been shown to promote p -type Hall behavior [61], and nonstoichiometric Gd-Vs produce strong negative magnetoresistance behavior at low fields ($\mu_0 H < 1$ T) as well as a smaller magnetoresistance [39].

The magnetoresistance at 14 T reaches a maximum value of 110% for a 10-nm-thick film at 1.8 K [Fig. 6(b)] and 10% for a 4-nm-thick film (Fig. S7), the latter being a high value for RE-Vs with a thickness < 5 nm [29,30]. Shubnikov-de Haas (SdH) oscillations were observed on top of the magnetoresistance background and were obtained by removing the background using a fifth-order polynomial fit (Fig. S5). The fast Fourier transform (FFT) of the quantum oscillations reveals three frequencies in Fig. 6(c), corresponding to the circular cross section of the ellipsoid electron pocket at the bulk X point along the film plane normal α_{\perp} (359 T) and the two hole pockets, namely, β (740 T) and δ (1564 T) at the Γ point. The Fermi surface of the electron pockets lying at the film (001) plane is not resolved in the FFT spectrum due to the high effective mass of the major-axis band (see Table I). Therefore, we have used the DFT-calculated aspect ratio of the elliptical electron pocket to estimate its Fermi volume. The FFT amplitude corresponding to the electron pocket α_{\perp} shows a single peak, despite significant exchange splitting. Further information on the SdH oscillations, magnetotransport models, as well as details on the absence of exchange spin-splitting signatures in the electron-pocket FFT frequencies are provided in the Appendix and Supplemental Material, Note 3 [45].

Carrier concentrations derived from SdH oscillations are provided in Table III. A similar disparity between ARPES and magnetotransport calculations was seen in earlier RE-Vs studies [28,52,53]. The lower Fermi wave vectors extracted from ARPES fits are explained by significant k_z broadening at the VUV wavelengths, leading to an underestimated Fermi surface area [36]. The carrier concentration calculated from both SdH oscillations and the magnetotransport multicarrier fit are in good agreement with previous values of $\sim 4.2 \cdot 10^{20}\text{cm}^{-3}$ found for GdSb bulk crystals [39]. A carrier compensation of $n_e/n_h = 0.67$ is calculated from the SdH oscillations, similar to the ARPES-extracted ratios, yet still far from the nearly exact charge compensation typically assumed for bulk RE-V crystals. Deviations from an exact carrier ratio $n_e/n_h = 1$ were measured in other bulk RE-V compounds such as DySb [62], LaBi [63], YSb [53], and NdSb [64]. Only a moderate level of compensation may be in fact needed for RE-V compounds

to exhibit XMR as long as the carrier mobilities are high. Additional causes for uncompensated carrier concentrations could be more systematic, as the calculations of carrier ratios from Fermi surfaces could depend on the Fermi volume estimation [27]. Lastly, the density of states values from the DFT calculation in Table S1 show nearly exact carrier compensation. Yet, the computed carrier densities in GdSb also depend significantly on the Fermi level position. A 50 meV shift would cause a relatively steep change in n_e/n_h from 0.7 to 1.5. RE-V thin films are more susceptible to quantum confinement effects and Fermi level shifts than bulk crystals due to potential charge transfer at the surface/interface.

Hall coefficients measured for bulk GdSb crystals have shown a transition from p - to n -type behavior near 5 K [39]. In contrast, in the 10- and 4-nm-thick films a consistent n -type behavior is measured in Fig. 6(d) and Fig. S7(c), indicating that either a carrier density mismatch or reduced hole mobility leads to a net negative Hall coefficient. Given the temperature dependence of the Hall coefficient at low temperatures < 10 K, the higher electron mobility likely leads to the n -type behavior.

In Fig. 7(a), the Kohler plot [65] shows the effect of magnetic scattering, mobility fluctuations, and electron-electron interactions on varying relaxation times. At low fields, the magnetoresistance behavior can be separated into two temperature regimes: low temperatures ($T \ll T_N$) and high temperatures ($T \sim T_N$, $T > T_N$). At low temperatures, spin scattering due to the spin-flop transition and quantum interference effects leads to a slower, nonparabolic rise in magnetoresistance observed up to ~ 2 T (~ 0.15 T/ $\mu\Omega$ cm). At high temperatures, quantum interference is suppressed, and spin scattering persists for all fields in the paramagnetic phase and results in a magnetoresistance scaling of $MR \propto (\mu_0 H / \rho_0)^{1.58}$, deviating from the ideal value of 2 due to potential carrier concentration and mobility imbalance.

High magnetic fields are expected to lead to strong exchange splitting at the electron pocket below T_N [see Fig. 7(b)], potentially leading to a change in carrier compensation. However, based on DFT calculations the ferromagnetic phase of GdSb remains charge compensated (Table II), indicating that no significant carrier concentration change is expected at $T < T_N$ at high magnetic fields.

Figures 7(c) and 7(d) show the temperature dependence of the charge-carrier mobilities obtained from simultaneously fitting the Hall and longitudinal magnetoresistance with a two-band model. The hole- and electron carrier density extracted from multiband fits to the magnetotransport data lies between the concentrations extracted from ARPES fits and SdH oscillations, showing an electron-rich carrier density at high temperatures and a nearly compensated carrier concentration below 10 K. This spread in the calculated carrier ratios compared to the other approaches reflects the limited accuracy a simple multicarrier model has in estimating carrier concentrations compared to the more direct methods employed earlier for studying the thin-film Fermi surface. More details on the magnetotransport multiband fit are provided in Supplemental Material, Note 3 [45].

In Fig. 7(c), the hole bands show a smaller Hall mobility than the electron pocket at low temperatures. The opposite occurs above the magnetic transition temperature, a trend also

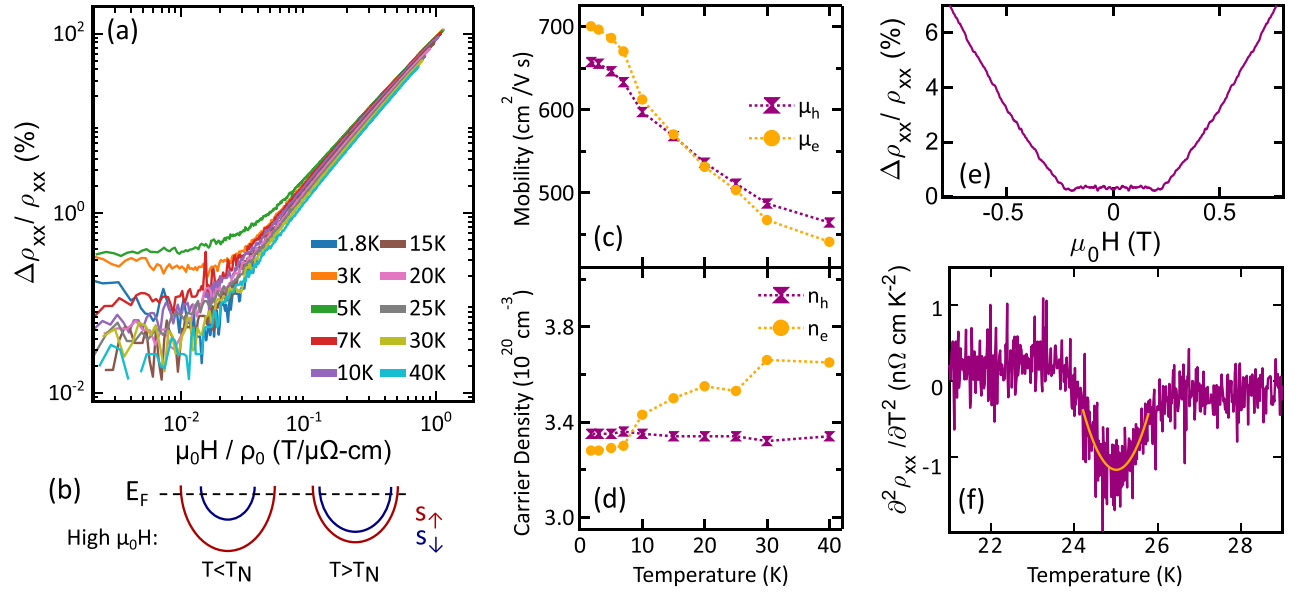


FIG. 7. (a) Kohler scaling of magnetoresistance. (b) Schematic of magnetic field-induced exchange interactions in the electron pocket. Temperature dependencies of the mobilities (c) of charge carriers and their concentration (d) extracted from a two-band fit as described in the main text. (e) Low magnetic field magnetoresistance at 1.8 K shows the spin-flop transition. (f) Néel temperature extracted from a parabolic fit to the second derivative of the resistivity at $B = 0$ T.

observed for bulk single crystals [39]. The higher electron mobility at low temperatures where scattering is reduced is consistent with observations of a smaller effective mass for the minor axis of the electron pocket vs the hole bands as measured by ARPES (Table I). After crossing T_N at 25 K to lower temperatures, an accelerated increase in carrier mobilities is seen in Fig. 7(c), in agreement with the expected suppressed magnetic scattering at low temperatures (mainly affecting the electrons due to strong d - f scattering). The mobility of electrons and holes shows only a gradual linear-like increase as the temperature drops below 7 K, unlike the nearly exponential rise in mobility observed for bulk Gd-V single crystals [39,66]. The mobility saturation at low temperatures suggests that interfacial roughness and surface scattering limit carrier mobilities.

From the temperature-dependent resistivity measurements plotted in Fig. 6(a), the kink and sharp drop in resistivity below the Néel temperature indicate that spin-disorder scattering significantly contributes to the total resistivity close to the Néel temperature. Evidence of the onset of exchange splitting in the spin-flop phase is provided in Fig. 7(e) by the plateaued magnetoresistance at low magnetic fields, which decreases around 0.2 T and begins to follow the expected linear/quadratic-like scaling [$MR \propto (\mu_0 H)^n$, $n = 1-2$] after crossing the spin-flop field [67]. T_N is extracted from the minima in the second-derivative resistivity plots, which are expected to diverge at the Néel temperature [see example fit in Fig. 7(f)] [44].

IV. CONCLUSIONS

In summary, we have grown epitaxial GdSb films by MBE and studied their band structure and magnetic properties with ARPES, DFT, and magnetotransport. The growth

window of high-quality single-crystal GdSb films on a lattice-matched III-V structure has been established, resulting in high magnetoresistance values for the given film thicknesses among RE-V. Our comprehensive study of GdSb films paves the way to understand the relationship between the electronic and transport properties of RE-Vs films vs their bulk crystals and other films in semimetallic systems with similar chemistry, such as the Heusler compounds: GdXV ($X = \text{Pt, Pd}$; $V = \text{Sb, Bi}$).

We have identified magnetic and interface scattering mechanisms in GdSb, limiting the mobilities of thin RE-V films and ultimately resulting in lower magnetoresistance values than bulk single crystals and reduced magnetoresistance in thinner films. ARPES experiments of the GdSb layer showed quantization effects of energy levels in the electron- and hole pockets. We did not detect these features in magnetotransport quantum oscillations due to the higher surface scattering and larger effective mass of the higher-energy quantum-well subband levels. Tuning the quantum-level subband energy position by varying the film thickness could serve as a potential route for engineering carrier compensation and mobilities for improved magnetoresistive behavior.

While we do not see evidence of a p - d band inversion in ARPES measurements performed for the antiferromagnetic state, our DFT calculations show the near onset of band overlap for strong exchange splitting at low temperatures and high magnetic fields in the forced ferromagnetic phase. DFT calculations treating the $4f$ electrons as core levels in a nonmagnetic phase describe well the band structure of GdSb below the Néel temperature. By introducing $4f$ electron AFM ordering into the valence-band structure in our DFT calculations, we have obtained a more accurate description of the split-off band position and total carrier density of the electron- and hole bands.

ACKNOWLEDGMENTS

Synthesis of thin films, development of a prototype ultrahigh-vacuum suitcase, ARPES experiments, and theoretical work were supported by the U.S. Department of Energy (Contract No. DE-SC0014388). Development of the growth facilities and low-temperature magnetotransport measurements were supported by the Office of Naval Research through the Vannevar Bush Faculty Fellowship under Award No. N00014-15-1-2845. Scanning probe studies were supported by NSF (Award No. DMR-1507875). This research used resources of the Advanced Light Source, which is a Department of Energy (DOE) Office of Science User Facility under Contract No. DE-AC02-05CH11231. Use of the Stanford Synchrotron Radiation Lightsources, SLAC National Accelerator Laboratory, is supported by the U.S. DOE, Office of Science, Office of Basic Energy Sciences under Contract No. DE-AC02-76SF00515. We acknowledge the use of shared facilities of the NSF Materials Research Science and Engineering Center (MRSEC) at the University of California Santa Barbara (Grant No. DMR 1720256). DFT calculations used the National Energy Research Scientific Computing Center (NERSC), a U.S. DOE Office of Science User Facility operated under Contract No. DE-AC02-05CH11231. H.S.I. gratefully acknowledges support from the UC Santa Barbara NSF Quantum Foundry funded via the Q-AMASE-i program under Award No. DMR-1906325 and support for further developments of the vacuum suitcases. D.Q.H. acknowledges support from NSF through the University of Delaware Materials Research Science and Engineering Center, Grant No. DMR-2011824. We thank Connor P. Dempsey, Elliot Young, and Maxwell Bocheff for technical assistance in measurements and in the construction of new ultrahigh-vacuum experimental setups.

APPENDIX: CARRIER-DENSITY VALUES

The experimental Fermi surface volumes in Tables I and III are calculated assuming an elliptical surface for the α bands, and spherical surfaces for the hole pockets. The total carrier density is calculated as discussed in Ref. [61]: $n_e =$

$3n_\alpha$, $n_h = n_\beta + n_\delta$, $n_{\alpha/\beta/\delta} = \frac{V_F}{4\pi^3}$, and $V_F^{\beta/\delta} = \frac{4\pi}{3}r^3$, $V_F^\alpha = \frac{4\pi}{3}(k_F^{\text{minor}})^2 k_F^{\text{major}}$, with the radius r for the hole pockets described below. The Fermi volume model accuracy was confirmed by calculating the carrier density from the DFT Fermi wave vectors in Table II (marked with *). The degree of compensation between the hole- and electron carriers was found to depend mainly on the approximated shape of the δ pocket Fermi volume, similar to earlier observations made for YSb [53] and other La-V compounds [27]. The nonspherical band warping in the heavy-hole δ band (and smaller distortion in the light-hole β band) is accounted for by investigating three possible Fermi surface shapes and selecting the model that best describes the DFT carrier density using the DFT Fermi wave vectors for the analytical calculation. The sphere model (b) below matches best the extracted density of states in Table II, and the two other models serve as lower and upper bounds for the carrier density:

(a) A Fermi surface composed of two opposite pyramids sharing a base. The pyramid square base area is $A^\delta = (2k_F(\delta_{\bar{X}} - \bar{\Gamma} - \bar{X}))^2$, the height is $h^\delta = k_F(\delta_{\bar{M}} - \bar{\Gamma} - \bar{M})$, and $n_{\delta(\text{DFT})} = 1.91 \times 10^{20} \text{ cm}^{-3}$.

(b) Sphere: The radius being $r = \frac{k_F(\delta_{\bar{X}} - \bar{\Gamma} - \bar{X}) + k_F(\delta_{\bar{M}} - \bar{\Gamma} - \bar{M})}{2}$ and a total volume $V_F = \frac{4\pi}{3}r^3$, $n_{\delta(\text{DFT})} = 3.62 \times 10^{20} \text{ cm}^{-3}$.

(c) Average volume of two spheres. $V_F = \frac{4\pi}{3} \frac{r_1^3 + r_2^3}{2}$, where $r_1 = k_F(\delta_{\bar{X}} - \bar{\Gamma} - \bar{X})$, $r_2 = k_F(\delta_{\bar{M}} - \bar{\Gamma} - \bar{M})$, and $n_{\delta(\text{DFT})} = 3.80 \times 10^{20} \text{ cm}^{-3}$.

The magnetotransport quantum oscillation carrier densities in Table III were calculated from the FFT frequency of the SdH oscillations f_{FFT} , using the Onsager relation: $f_{\text{FFT}} = \frac{\Phi_0 A_{\text{ext}}}{2\pi^2}$. Φ_0 is the magnetic flux quantum, and A_{ext} is the extremal orbit area for α_\perp , β , δ , assumed to be circular: $A_{\text{ext}} = \pi k_F^2$. We extract the electron-pocket semimajor Fermi wave vector, $k_F(\alpha_{\text{minor}})$, and the hole pockets $k_F(\beta)$ and $k_F(\delta)$. The electron pocket $k_F(\alpha_{\text{major}})$ is calculated assuming an ellipsoidal band with a wave-vector ratio of $\frac{k_F(\alpha_{\text{major}})}{k_F(\alpha_{\text{minor}})} = \frac{3.79}{1}$ (derived from the DFT k_F ratio in the AFM phase; see Table II). The Fermi surface volumes are then calculated from the SdH Fermi wave vectors as described earlier.

-
- [1] I. A. Leahy, Y.-P. Lin, P. E. Siegfried, A. C. Treglia, J. C. W. Song, R. M. Nandkishore, and M. Lee, *Proc. Natl. Acad. Sci.* **115**, 10570 (2018).
- [2] J. Lenz and S. Edelstein, *IEEE Sens. J.* **6**, 631 (2006).
- [3] J. Hu, S.-Y. Xu, N. Ni, and Z. Mao, *Annu. Rev. Mater. Res.* **49**, 207 (2019).
- [4] I. Vobornik, A. B. Sarkar, L. Zhang, D. W. Boukhvalov, B. Ghosh, L. Piliari, C. Kuo, D. Mondal, J. Fujii, C. S. Lue, M. Vorokhta, H. Xing, L. Wang, A. Agarwal, and A. Politano, *Adv. Funct. Mater.* **31**, 2106101 (2021).
- [5] L. Šmejkal, T. Jungwirth, and J. Sinova, *Phys. Status Solidi RRL* **11**, 1700044 (2017).
- [6] D.-F. Shao, G. Gurung, S.-H. Zhang, and E. Y. Tsymlal, *Phys. Rev. Lett.* **122**, 077203 (2019).
- [7] Q. Shao, P. Li, L. Liu, H. Yang, S. Fukami, A. Razavi, H. Wu, K. Wang, F. Freimuth, Y. Mokrousov, M. D. Stiles, S. Emori, A. Hoffmann, J. Akerman, K. Roy, J.-P. Wang, S.-H. Yang, K. Garello, and W. Zhang, *IEEE Trans. Magn.* **57**, 1 (2021).
- [8] J. Tian, I. Childres, H. Cao, T. Shen, I. Miotkowski, and Y. P. Chen, *Solid State Commun.* **191**, 1 (2014).
- [9] V. Baltz, A. Manchon, M. Tsoi, T. Moriyama, T. Ono, and Y. Tserkovnyak, *Rev. Mod. Phys.* **90**, 015005 (2018).
- [10] P. Němec, M. Fiebig, T. Kampfrath, and A. V. Kimel, *Nat. Phys.* **14**, 229 (2018).
- [11] T. Matsuda, N. Kanda, T. Higo, N. P. Armitage, S. Nakatsuji, and R. Matsunaga, *Nat. Commun.* **11**, 1 (2020).
- [12] L. Zhang, C. Guo, C.-N. Kuo, H. Xu, K. Zhang, B. Ghosh, J. De Santis, D. W. Boukhvalov, I. Vobornik, V. Paolucci, C. S. Lue,

- H. Xing, A. Agarwal, L. Wang, and A. Politano, *Phys. Status Solidi RRL* **15**, 2100212 (2021).
- [13] R. Xie, T. Zhang, H. Weng, and G.-L. Chai, *Small Sci.* **2**, 2100106 (2022).
- [14] C. Biz, M. Fianchini, and J. Gracia, *ACS Catal.* **11**, 14249 (2021).
- [15] W. Mtangi, V. Kiran, C. Fontanesi, and R. Naaman, *J. Phys. Chem. Lett.* **6**, 4916 (2015).
- [16] C. J. Palmstrøm, N. Tabatabaie, and S. J. Allen, *Appl. Phys. Lett.* **53**, 2608 (1988).
- [17] C. J. Palmstrøm, S. Mounier, T. G. Finstad, and P. F. Miceli, *Appl. Phys. Lett.* **56**, 382 (1990).
- [18] T. Sands, C. J. Palmstrøm, J. P. Harbison, V. G. Keramidas, N. Tabatabaie, T. L. Cheeks, R. Ramesh, and Y. Silberberg, *Mater. Sci. Rep.* **5**, 99 (1990).
- [19] F. F. Tafti, Q. D. Gibson, S. K. Kushwaha, N. Haldolaarachchige, and R. J. Cava, *Nat. Phys.* **12**, 272 (2016).
- [20] J. Nayak, S. C. Wu, N. Kumar, C. Shekhar, S. Singh, J. Fink, E. E. D. Rienks, G. H. Fecher, S. S. P. Parkin, B. Yan, and C. Felser, *Nat. Commun.* **8**, 13942 (2017).
- [21] B. Schruck, Y. Kushnirenko, B. Kuthanazhi, J. Ahn, L. L. Wang, E. O'Leary, K. Lee, A. Eaton, A. Fedorov, R. Lou, V. Voroshnin, O. J. Clark, J. Sánchez-Barriga, S. L. Bud'ko, R. J. Slager, P. C. Canfield, and A. Kaminski, *Nature (London)* **603**, 610 (2022).
- [22] S. Jang, R. Kealhofer, C. John, S. Doyle, J. Hong, J. H. Shim, Q. Si, O. Erten, J. D. Denlinger, and G. J., *Analytis, Sci. Adv.* **5**, eaat7158 (2019).
- [23] C. J. Palmstrøm, *Annu. Rev. Mater. Sci.* **25**, 389 (1995).
- [24] C. C. Bomberger, M. R. Lewis, L. R. Vanderhoef, M. F. Doty, and J. M. O. Zide, *J. Vac. Sci. Technol. B* **35**, 030801 (2017).
- [25] S. A. Solin, T. Thio, D. R. Hines, and J. J. Heremans, *Science* **289**, 1530 (2000).
- [26] M. Holz, O. Kronenwerth, and D. Grundler, *Phys. Rev. B* **67**, 195312 (2003).
- [27] H.-Y. Yang, T. Nummy, H. Li, S. Jaszewski, M. Abramchuk, D. S. Dessau, and F. Tafti, *Phys. Rev. B* **96**, 235128 (2017).
- [28] J. Xu, N. J. Ghimire, J. S. Jiang, Z. L. Xiao, A. S. Botana, Y. L. Wang, Y. Hao, J. E. Pearson, and W. K. Kwok, *Phys. Rev. B* **96**, 075159 (2017).
- [29] S. Chatterjee, S. Khalid, H. S. Inbar, A. Goswami, T. Guo, Y.-H. Chang, E. Young, A. V. Fedorov, D. Read, A. Janotti, and C. J. Palmstrøm, *Sci. Adv.* **7**, eabe8971 (2021).
- [30] H. Inoue, M. Han, M. Hu, T. Suzuki, J. Liu, and J. G. Checkelsky, *Phys. Rev. Mater.* **3**, 101202(R) (2019).
- [31] T. Schumann, M. Goyal, D. A. Kealhofer, and S. Stemmer, *Phys. Rev. B* **95**, 241113(R) (2017).
- [32] E. M. Krivoy, S. Rahimi, H. P. Nair, R. Salas, S. J. Maddox, D. J. Ironside, Y. Jiang, V. D. Dasika, D. A. Ferrer, G. Kelp, G. Shvets, D. Akinwande, and S. R. Bank, *Appl. Phys. Lett.* **101**, 221908 (2012).
- [33] N. L. Eatough and H. T. Hall, *Inorg. Chem.* **8**, 1439 (1969).
- [34] P. Li, Z. Wu, F. Wu, C. Cao, C. Guo, Y. Wu, Y. Liu, Z. Sun, C.-M. Cheng, D.-S. Lin, F. Steglich, H. Yuan, T.-C. Chiang, and Y. Liu, *Phys. Rev. B* **98**, 085103 (2018).
- [35] T. J. Nummy, J. A. Waugh, S. P. Parham, Q. Liu, H.-Y. Yang, H. Li, X. Zhou, N. C. Plumb, F. F. Tafti, and D. S. Dessau, *npj Quantum Mater.* **3**, 24 (2018).
- [36] K. Kuroda, M. Ochi, H. S. Suzuki, M. Hirayama, M. Nakayama, R. Noguchi, C. Bareille, S. Akebi, S. Kunisada, T. Muro, M. D. Watson, H. Kitazawa, Y. Haga, T. K. Kim, M. Hoesch, S. Shin, R. Arita, and T. Kondo, *Phys. Rev. Lett.* **120**, 086402 (2018).
- [37] S. Khalid, F. P. Sabino, and A. Janotti, *Phys. Rev. B* **98**, 220102(R) (2018).
- [38] S. Khalid and A. Janotti, *Phys. Rev. B* **102**, 035151 (2020).
- [39] D. X. Li, Y. Haga, H. Shida, T. Suzuki, and Y. S. Kwon, *Phys. Rev. B* **54**, 10483 (1996).
- [40] B. D. Schultz, H. H. Farrell, M. M. R. Evans, K. Lüdge, and C. J. Palmstrøm, *J. Vac. Sci. Technol. B Microelectron. Nanom. Struct.—Process., Meas., Phenom.* **20**, 1600 (2002).
- [41] J. K. Kawasaki, R. Timm, K. T. Delaney, E. Lundgren, A. Mikkelsen, and C. J. Palmstrøm, *Phys. Rev. Lett.* **107**, 036806 (2011).
- [42] E. M. Krivoy, A. P. Vasudev, S. Rahimi, R. A. Synowicki, K. M. McNicholas, D. J. Ironside, R. Salas, G. Kelp, D. Jung, H. P. Nair, G. Shvets, D. Akinwande, M. L. Lee, M. L. Brongersma, and S. R. Bank, *ACS Photonics* **5**, 3051 (2018).
- [43] D. X. Li, Y. Haga, H. Shida, T. Suzuki, Y. S. Kwon, and G. Kido, *J. Phys.: Condens. Matter* **9**, 10777 (1997).
- [44] H. Taub and S. J. Williamson, *Solid State Commun.* **13**, 1021 (1973).
- [45] See Supplemental Material at <http://link.aps.org/supplemental/10.1103/PhysRevMaterials.6.L121201> for details about (a) MBE growth of GdSb and surface characterization, (b) ARPES data analysis and DFT calculations, (c) SdH oscillations, magnetotransport models, and exchange spin splitting, and (d) magnetotransport in thinner films. See also Refs. [56,68–81] therein.
- [46] H. Yamada, T. Fukawa, T. Muro, Y. Tanaka, S. Imada, S. Suga, D.-X. Li, and T. Suzuki, *J. Phys. Soc. Jpn.* **65**, 1000 (1996).
- [47] J. Heyd, G. E. Scuseria, and M. Ernzerhof, *J. Chem. Phys.* **118**, 8207 (2003).
- [48] J. Heyd, G. E. Scuseria, and M. Ernzerhof, *J. Chem. Phys.* **124**, 219906 (2006).
- [49] G. Kresse and J. Hafner, *Phys. Rev. B* **47**, 558 (1993).
- [50] G. Kresse and J. Hafner, *Phys. Rev. B* **49**, 14251 (1994).
- [51] B. D. Schultz, S. G. Choi, and C. J. Palmstrøm, *Appl. Phys. Lett.* **88**, 243117 (2006).
- [52] Z. Wu, F. Wu, P. Li, C. Guo, Y. Liu, Z. Sun, C. M. Cheng, T. C. Chiang, C. Cao, H. Yuan, and Y. Liu, *Phys. Rev. B* **99**, 035158 (2019).
- [53] J. He, C. Zhang, N. J. Ghimire, T. Liang, C. Jia, J. Jiang, S. Tang, S. Chen, Y. He, S.-K. Mo, C. C. Hwang, M. Hashimoto, D. H. Lu, B. Moritz, T. P. Devereaux, Y. L. Chen, J. F. Mitchell, and Z.-X. Shen, *Phys. Rev. Lett.* **117**, 267201 (2016).
- [54] Y. Wu, Y. Lee, T. Kong, D. Mou, R. Jiang, L. Huang, S. L. Bud'ko, P. C. Canfield, and A. Kaminski, *Phys. Rev. B* **96**, 035134 (2017).
- [55] J. K. Kawasaki, C. H. Kim, J. N. Nelson, S. Crisp, C. J. Zollner, E. Biegenwald, J. T. Heron, C. J. Fennie, D. G. Schlom, and K. M. Shen, *Phys. Rev. Lett.* **121**, 176802 (2018).
- [56] N. Trivedi and N. W. Ashcroft, *Phys. Rev. B* **38**, 12298 (1988).
- [57] X. Duan, F. Wu, J. Chen, P. Zhang, Y. Liu, H. Yuan, and C. Cao, *Commun. Phys.* **1**, 71 (2018).
- [58] J. A. Sobota, K. Kim, H. Takatsu, M. Hashimoto, S.-K. Mo, Z. Hussain, T. Oguchi, T. Shishidou, Y. Maeno, B. I. Min, and Z.-X. Shen, *Phys. Rev. B* **88**, 125109 (2013).

- [59] T. Kasuya and D. X. Li, *J. Magn. Magn. Mater.* **166**, (1997).
- [60] D. X. Li, Y. Haga, H. Shida, and T. Suzuki, *J. Appl. Phys.* **80**, 264 (1996).
- [61] S. Chatterjee, S. Khalid, H. S. Inbar, A. Goswami, F. C. de Lima, A. Sharan, F. P. Sabino, T. L. Brown-Heft, Y.-H. Chang, A. V. Fedorov, D. Read, A. Janotti, and C. J. Palmström, *Phys. Rev. B* **99**, 125134 (2019).
- [62] D. D. Liang, Y. J. Wang, C. Y. Xi, W. L. Zhen, J. Yang, L. Pi, W. K. Zhu, and C. J. Zhang, *APL Mater.* **6**, 086105 (2018).
- [63] J. Jiang, N. B. M. Schröter, S.-C. Wu, N. Kumar, C. Shekhar, H. Peng, X. Xu, C. Chen, H. F. Yang, C.-C. Hwang, S.-K. Mo, C. Felser, B. H. Yan, Z. K. Liu, L. X. Yang, and Y. L. Chen, *Phys. Rev. Mater.* **2**, 024201 (2018).
- [64] Y. Wang, J. H. Yu, Y. Q. Wang, C. Y. Xi, L. S. Ling, S. L. Zhang, J. R. Wang, Y. M. Xiong, T. Han, H. Han, J. Yang, J. Gong, L. Luo, W. Tong, L. Zhang, Z. Qu, Y. Y. Han, W. K. Zhu, L. Pi, X. G. Wan, C. Zhang, and Y. Zhang, *Phys. Rev. B* **97**, 115133 (2018).
- [65] J. M. Ziman, *Electrons and Phonons: The Theory of Transport Phenomena in Solids* (Oxford University Press, Oxford, 2001).
- [66] L. Ye, T. Suzuki, C. R. Wicker, and J. G. Checkelsky, *Phys. Rev. B* **97**, 081108(R) (2018).
- [67] S. J. Allen, N. Tabatabaie, C. J. Palmström, G. W. Hull, T. Sands, F. DeRosa, H. L. Gilchrist, and K. C. Garrison, *Phys. Rev. Lett.* **62**, 2309 (1989).
- [68] K. Jousten, F. Boineau, N. Bundaleski, C. Illgen, J. Setina, O. M. N. D. Teodoro, M. Vicar, and M. Wüest, *Vacuum* **179**, 109545 (2020).
- [69] P. D. C. King, T. D. Veal, and C. F. McConville, *Phys. Rev. B* **77**, 125305 (2008).
- [70] P. Hohenberg and W. Kohn, *Phys. Rev.* **136**, B864 (1964).
- [71] W. Kohn and L. J. Sham, *Phys. Rev.* **140**, A1133 (1965).
- [72] P. E. Blöchl, *Phys. Rev. B* **50**, 17953 (1994).
- [73] V. Popescu and A. Zunger, *Phys. Rev. Lett.* **104**, 236403 (2010).
- [74] V. Popescu and A. Zunger, *Phys. Rev. B* **85**, 085201 (2012).
- [75] P. M. C. Rourke and S. R. Julian, *Comput. Phys. Commun.* **183**, 324 (2012).
- [76] G. Pizzi, V. Vitale, R. Arita, S. Blügel, F. Freimuth, G. Géranton, M. Gibertini, D. Gresch, C. Johnson, T. Koretsune, J. Ibañez-Azpiroz, H. Lee, J.-M. Lihm, D. Marchand, A. Marrazzo, Y. Mokrousov, J. I. Mustafa, Y. Nohara, Y. Nomura, L. Paulatto, S. Poncé, T. Ponweiser, J. Qiao, F. Thöle, S. S. Tsirkin, M. Wierzbowska, N. Marzari, D. Vanderbilt, I. Souza, A. A. Mostofi, and J. R. Yates, *J. Phys.: Condens. Matter* **32**, 165902 (2020).
- [77] R. Daou, A. Haase, M. Doerr, M. Rotter, F. Weickert, M. Nicklas, and F. Steglich, *J. Phys. Conf. Ser.* **273**, 012111 (2011).
- [78] Y. Nakanishi, T. Sakon, M. Motokawa, M. Ozawa, and T. Suzuki, *Phys. Rev. B* **69**, 024412 (2004).
- [79] G. Dwari, S. Sasmal, B. Maity, V. Saini, R. Kulkarni, and A. Thamizhavel, [arXiv:2111.13836](https://arxiv.org/abs/2111.13836).
- [80] N. V. Kozlova, N. Mori, O. Makarovskiy, L. Eaves, Q. D. Zhuang, A. Krier, and A. Patanè, *Nat. Commun.* **3**, 1097 (2012).
- [81] H. Y. Yang, J. Gaudet, A. A. Aczel, D. E. Graf, P. Blaha, B. D. Gaulin, and F. Tafti, *Phys. Rev. B* **98**, 045136 (2018).